

Exploring 4D quantum Hall physics with a 2D topological charge pump

Michael Lohse^{1,2}, Christian Schweizer^{1,2}, Hannah M. Price^{3,4}, Oded Zilberberg⁵ & Immanuel Bloch^{1,2}

The discovery of topological states of matter has greatly improved our understanding of phase transitions in physical systems. Instead of being described by local order parameters, topological phases are described by global topological invariants and are therefore robust against perturbations. A prominent example is the two-dimensional (2D) integer quantum Hall effect¹: it is characterized by the first Chern number, which manifests in the quantized Hall response that is induced by an external electric field². Generalizing the quantum Hall effect to four-dimensional (4D) systems leads to the appearance of an additional quantized Hall response, but one that is nonlinear and described by a 4D topological invariant—the second Chern number^{3,4}. Here we report the observation of a bulk response with intrinsic 4D topology and demonstrate its quantization by measuring the associated second Chern number. By implementing a 2D topological charge pump using ultracold bosonic atoms in an angled optical superlattice, we realize a dynamical version of the 4D integer quantum Hall effect^{5,6}. Using a small cloud of atoms as a local probe, we fully characterize the nonlinear response of the system via *in situ* imaging and site-resolved band mapping. Our findings pave the way to experimentally probing higher-dimensional quantum Hall systems, in which additional strongly correlated topological phases, exotic collective excitations and boundary phenomena such as isolated Weyl fermions are predicted⁴.

Topology, originally a branch of mathematics, has become an important concept in different fields of physics, including particle physics⁷, solid-state physics⁸ and quantum computation⁹. In this context, a hallmark achievement was the discovery of the 2D integer quantum Hall effect¹. This discovery demonstrated that the Hall conductance in a perpendicular magnetic field and in response to an electric field E is quantized. In a cylindrical geometry, following Laughlin's thought experiment, E can be generated by varying the time-dependant magnetic flux $\phi_x(t)$ along the axis (x) of the cylinder¹⁰ (Fig. 1a). The interplay between the perpendicular magnetic field and the induced electric field E_z creates a quantized Hall response in the x direction: an integer number of particles, determined by the first Chern number, is transported between the edges per quantum of magnetic flux that is threaded through the cylinder².

Dimensionality is crucial for topological phases and many intriguing states were recently discovered in three dimensions, such as Weyl semimetals^{11,12} and three-dimensional (3D) topological insulators¹³. Ascending further in dimensions, a 4D generalization of the quantum Hall effect has been proposed in the context of astrophysics³ and condensed-matter systems⁴, and has received much attention in theoretical studies⁸. Unlike its 2D equivalent, the 4D quantum Hall effect can occur in systems with and without time-reversal symmetry^{3,4}. The former constitutes the fundamental model from which many lower-dimensional time-reversal-symmetric topological insulators can be derived^{8,14}. Furthermore, a 4D quantum Hall system might exhibit relativistic collective hyperedge excitations and new strongly correlated quantum Hall phases, revealing the interplay between quantum correlations and dimensionality⁴. This interest was renewed recently as

a result of the unprecedented control and flexibility made possible by engineered systems such as ultracold atoms and photonics. Such systems have been used to study various topological effects^{15,16}, including a measurement of the second Chern number in an artificially generated parameter space¹⁷, and offer a direct route for realizing 4D physics using synthetic dimensions^{18–20}.

In the simplest case, a 4D quantum Hall system can be composed of two 2D quantum Hall systems in orthogonal subspaces (Fig. 1a, b). In addition to the quantized linear response that underlies the 2D quantum Hall effect, a 4D quantum Hall system exhibits a quantized nonlinear 4D Hall response⁶. The latter arises when—simultaneously with the perturbing electric field E —a magnetic perturbation B is added. The 4D geometry implies multiple possibilities for the orientation of E and B ; however, the resulting nonlinear response is always characterized by the same 4D topological invariant, the second Chern number. Here, we focus on the geometry depicted in Fig. 1a, b, in which the nonlinear response can be understood semi-classically as originating from a Lorentz force created by B , which couples the motion in the two 2D quantum Hall systems²¹. The direction of this response is transverse to both perturbing fields. Hence, it can occur only in four or more dimensions and has therefore never been observed in any physical system.

Topological charge pumps exhibit topological transport properties that are similar to higher-dimensional quantum Hall systems and provide a way to probe 4D quantum Hall physics in lower-dimensional dynamical systems. The first example of a topological charge pump was the one-dimensional (1D) Thouless pump⁵, in which an adiabatic periodic modulation generates a quantized particle transport. This modulation can be parameterized by a pump parameter and, at each point in the cycle, the 1D system constitutes a Fourier component of a 2D quantum Hall system^{14,22}. The induced motion is thus equivalent to the linear Hall response and is characterized by the same 2D topological invariant, the first Chern number. Indeed, the quantum Hall effect on a cylinder can be mapped to a 1D charge pump with the threaded magnetic flux ϕ_x acting as the pump parameter¹⁰ (Fig. 1a). Building on early condensed-matter experiments²³, topological charge pumps have recently been realized in photonic waveguides²⁴ and by using ultracold atoms^{25,26}.

A dynamical 4D quantum Hall effect can accordingly be realized by using a 2D topological charge pump⁶. Using dimensional reduction^{14,22}, the Fourier components of a 4D quantum Hall system can be mapped onto a 2D system. For the geometry in Fig. 1a, b, the corresponding 2D model is a square superlattice (Fig. 1c, Methods), which consists of two 1D superlattices along the x and y directions, each formed by superimposing two lattices: $V_{s,\mu}\sin^2(\pi\mu/d_{s,\mu}) + V_{l,\mu}\sin^2(\pi\mu/d_{l,\mu} - \varphi_\mu/2)$, with $\mu \in \{x, y\}$. Here, $d_{s,\mu}$ and $d_{l,\mu} > d_{s,\mu}$ denote the period of the short and long lattices, respectively, and $V_{s,\mu}$ and $V_{l,\mu}$ the depths of the short and long lattice potentials. The position of the long lattice is determined by the corresponding superlattice phase φ_μ .

The phase φ_x is chosen as the pump parameter; that is, pumping is performed by moving the long lattice along x . This method of pumping

¹Fakultät für Physik, Ludwig-Maximilians-Universität, Schellingstraße 4, 80799 München, Germany. ²Max-Planck-Institut für Quantenoptik, Hans-Kopfermann-Straße 1, 85748 Garching, Germany. ³INO-CNR BEC Center and Dipartimento di Fisica, Università di Trento, Via Sommarive 14, 38123 Povo, Italy. ⁴School of Physics and Astronomy, University of Birmingham, Edgbaston, Birmingham B15 2TT, UK. ⁵Institut für Theoretische Physik, ETH Zürich, Wolfgang-Pauli-Straße 27, 8093 Zürich, Switzerland.

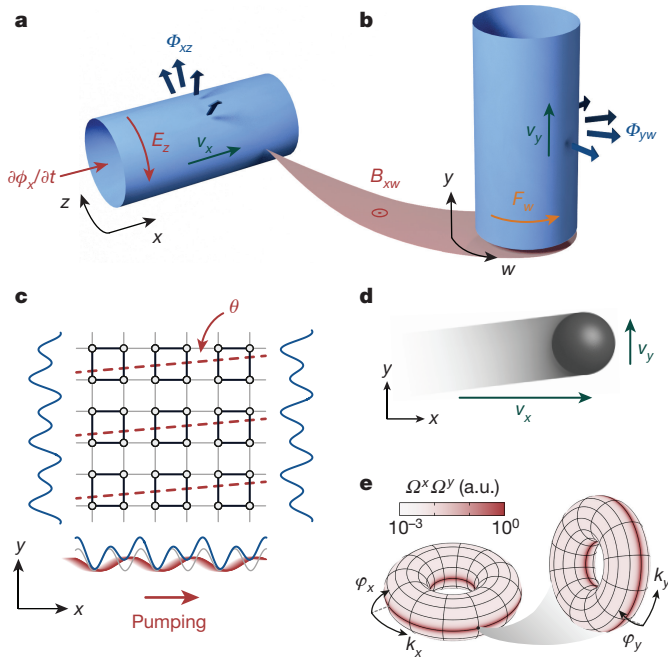


Figure 1 | 4D quantum Hall system and the corresponding 2D topological charge pump. **a**, A 2D quantum Hall system on a cylinder pierced by a uniform magnetic flux Φ_{xz} (blue arrows). Threading a magnetic flux $\phi_x(t)$ through the cylinder creates an electric field E_z on the surface (red arrows), resulting in a linear Hall response along x with velocity v_x (green arrow). **b**, A 4D quantum Hall system can be composed of two 2D quantum Hall systems in the x - z and y - w planes. A weak magnetic perturbation B_{xw} in the x - w plane couples the two systems and generates a Lorentz force F_w (orange arrow) for particles moving along x . This force induces an additional nonlinear Hall response in the y direction with velocity v_y (green arrow). **c**, A dynamical version of the 4D quantum Hall system can be realized by using a topological charge pump in a 2D superlattice (blue potentials). Such a superlattice is created by superimposing two lattices with periods d_s (grey) and $d_l > d_s$ (red) along both x and y , depicted here for $d_l = 2d_s$, as in the experiment. The black circles show the lattice sites that are formed by the potential minima, and the black (grey) lines indicate strong (weak) tunnel coupling between neighbouring sites. The system is modulated periodically by moving the long lattice adiabatically along x , mimicking the perturbing electric field E_z in the 4D model. The magnetic perturbation B_{xw} maps onto a small tilt angle θ of the long lattice along y with respect to the corresponding short lattice. In this case, the shape of the double wells along y depends on the position along x . The dashed red lines indicate the potential minima of the tilted long lattice. **d**, The pumping shifts the cloud of atoms (grey) in the x direction (with velocity v_x), as per the quantized linear response of a 2D quantum Hall system. For non-zero θ , the two orthogonal axes are coupled, leading to an additional quantized nonlinear response with 4D topology in the perpendicular y direction (with velocity v_y). **e**, The velocity of the nonlinear response is determined by the product of the Berry curvatures $\Omega^x \Omega^y$ (see Methods; a.u., arbitrary units), depicted here for the lowest subband with $d_l = 2d_s$ and lattice depths as in Fig. 3. The left (right) torus shows a cut at $k_y = 0$, $\varphi_y = \pi/2$ ($k_x = \pi/(2d_l)$, $\varphi_x = \pi/2$) through the generalized 4D Brillouin zone spanned by k_x , φ_x , k_y and φ_y .

is equivalent to threading the flux ϕ_x in the 4D model, leading to a quantized motion along x (the linear response; Fig. 1c, d). The magnetic perturbation B_{xw} corresponds to a transverse phase φ_y that depends linearly on x and thereby couples the motion in the x and y directions (see Methods). We realize this by tilting the long y lattice relative to the short one by an angle $\theta \ll 1$ (Fig. 1c) such that $\varphi_y(x) = \varphi_y^{(0)} + 2\pi\theta x/d_{l,y}$ to first order in θ . When φ_x is varied, the motion along x changes φ_y and—analogously to the Lorentz force in 4D—induces a quantized nonlinear response along y , which is equivalent to the nonlinear Hall response of a 4D quantum Hall system⁶ (Fig. 1c, d).

For a uniformly populated band in an infinite system, the centre-of-mass (COM) displacement during one cycle $\varphi_x = 0 \rightarrow 2\pi$ is

$$\nu_1^x a_x \mathbf{e}_x + \nu_2 \theta \frac{a_x}{d_{l,y}} a_y \mathbf{e}_y$$

with a_x (a_y) the size of the superlattice unit cell and \mathbf{e}_x (\mathbf{e}_y) the unit vector along x (y) (see Methods). The first term describes the quantized linear response along x . It is proportional to the first Chern number of the pump (ν_1^x ; denoted ν in ref. 31), which is obtained by integrating the Berry curvature

$$\Omega^x(k_x, \varphi_x) = i(\langle \partial_{\varphi_x} u | \partial_{k_x} u \rangle - \langle \partial_{k_x} u | \partial_{\varphi_x} u \rangle)$$

over the generalized 2D Brillouin zone spanned by the quasi-momentum k_x and φ_x . Here, $|u(k_x, \varphi_x)\rangle$ denotes the eigenstate of a given non-degenerate band at k_x and φ_x . Because ν_1^x can take only integer values, the motion is quantized²⁵. The second term is the nonlinear response in the y direction. It is quantified by a 4D integer topological invariant, the second Chern number of the pump (denoted ν in ref. 31):

$$\nu_2 = \frac{1}{4\pi^2} \oint_{\text{BZ}} \Omega^x \Omega^y dk_x dk_y d\varphi_x d\varphi_y$$

where BZ indicates the generalized 4D Brillouin zone (Fig. 1e). Therefore, the nonlinear response is also quantized and has intrinsic 4D symmetries that result from the higher-dimensional non-commutative geometry.

We implement a 2D topological charge pump by using bosonic ⁸⁷Rb atoms that form a Mott insulator in isolated planes of a 3D optical lattice with superlattices along x and y , with $d_s \equiv d_{s,x} = d_{s,y}$ and $d_l \equiv d_{l,x} = d_{l,y} = 2d_s$ (see Methods), creating double-well potentials along x and y (Fig. 1c). In the tight-binding limit, this implementation realizes a 2D Rice–Mele model²⁷ in each plane with dimerized on-site energies and tunnel couplings between neighbouring sites in both directions (see Methods). The corresponding unit cell is a four-site plaquette, $a_x = a_y = 2d_s$, and the lowest band splits into four subbands.

In the experiment, we study the nonlinear response of the lowest subband, for which $\nu_2 = +1$ for $d_l = 2d_s$. Our main results are: (i) the observation of a 4D-like bulk response; (ii) the local probing of its 4D geometric properties; and (iii) the revealing of the 4D quantum Hall effect by demonstrating the quantization of the response. As the initial state, a quarter-filled Mott insulator that uniformly occupies the lowest subband is prepared at $\varphi_x = 0$ (see Methods). The pumping is performed along x by adiabatically varying φ_x ; we examine the resulting motion of the atoms. We probe the system locally by using a small cloud of atoms that extends over approximately 20 sites in the x direction. In this case, the variation in $\Omega^y(\varphi_y)$ over the cloud is negligible and the y displacement per cycle is given by $\bar{\Omega}^y(\varphi_y^{(0)}) \theta a_x a_y / d_l$, with

$$\bar{\Omega}^y = \frac{1}{2\pi} \oint \Omega^x \Omega^y dk_x dk_y d\varphi_x$$

(see Methods). From this local response, the quantized nonlinear response of an infinite system can be reconstructed by sampling all $\varphi_y^{(0)} \in [0, 2\pi)$, thereby integrating over the entire 4D Brillouin zone. To probe the motion of the cloud, we measure its COM position as a function of φ_x . Because the nonlinear response results from two weak perturbations, the displacement per cycle is typically only a fraction of d_l . It is therefore too small to be resolved experimentally, because the number of experimental cycles is limited by heating. However, for suitable lattice parameters, signatures of the nonlinear drift—the key feature of the 4D Hall effect—can be seen at $\varphi_y^{(0)} = \pi/2$ (Fig. 2), at which $\bar{\Omega}^y$ is strongly peaked (see Fig. 1e). Unlike the linear response, this motion depends on θ , demonstrating the intrinsically 4D character of the nonlinear response, which results from the two independent perturbations in orthogonal subspaces. This result demonstrates the existence of this dynamical, transverse, bulk phenomenon directly.

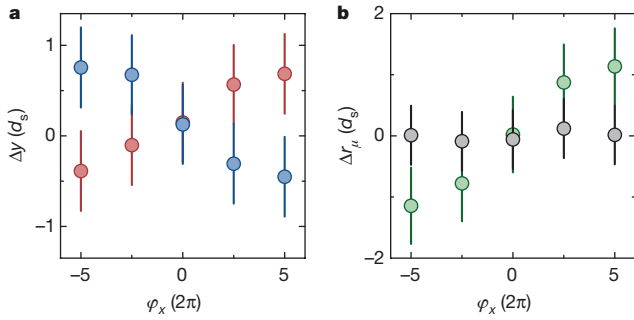


Figure 2 | 4D-like nonlinear centre-of-mass (COM) response. **a**, Shift in the COM of the cloud of atoms along y (Δy) versus the number of pump cycles along x (represented by φ_x) measured for two different angles, $\theta_1 = 0.78(2)$ mrad (red) and $\theta_2 = -0.85(2)$ mrad (blue), with $\varphi_y^{(0)} = 0.500(5)\pi$. When pumping along x , the cloud moves in the perpendicular y direction with the sign depending on the pumping direction and the sign of θ . Δy is the differential displacement for $V_{s,x} = 7.0(2)E_{r,s}$, $V_{s,y} = 17.0(5)E_{r,s}$, $V_{l,x} = 20.0(6)E_{r,l}$ and $V_{l,y} = 80(3)E_{r,l}$ compared to a reference sequence with $V_{s,y} = 40(1)E_{r,s}$ and $V_{l,y} = 0E_{r,l}$ (see Methods). Here $E_{r,i} = \hbar^2/(8m_a d_i^2)$, with $i \in \{s, l\}$, denotes the corresponding recoil energy, with m_a the mass of an atom. Each point is averaged 100 times and the error bar takes into account the error of the mean as well as a systematic uncertainty of $\pm 0.3d_s$. **b**, Difference in the COM drift between θ_1 and θ_2 for the x (grey) and y (green) directions: $\Delta r_\mu = \Delta\mu(\theta_1) - \Delta\mu(\theta_2)$, with $\mu \in \{x, y\}$. The direction of the nonlinear response reverses when changing the sign of θ , whereas the linear response is independent of θ . Data are calculated from the measurements in **a** (see Methods).

To quantify this nonlinear response, instead of *in situ* imaging we use site-resolved band mapping, which measures the number of atoms on even (N_e) and odd (N_o) sites along y . This method enables us to determine the average double-well imbalance, $\mathcal{I}_y = (N_o - N_e)/(N_o + N_e)$, accurately. If no transitions between neighbouring unit cells along y occur, then \mathcal{I}_y is related directly to the COM motion (see Methods).

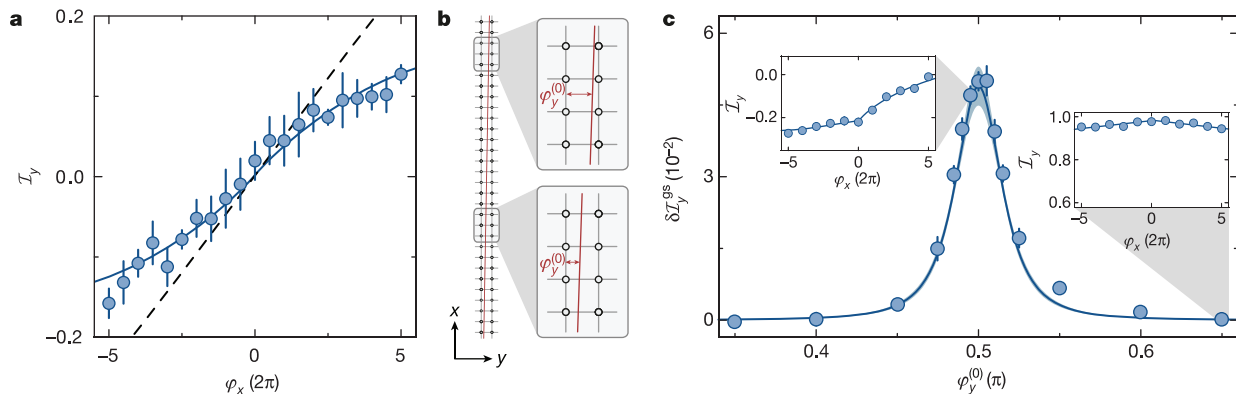


Figure 3 | Local probing of the quantized nonlinear bulk response for $\theta = 0.54(3)$ mrad. **a**, Double-well imbalance \mathcal{I}_y versus the number of pump cycles in the x direction at $\varphi_y^{(0)} = 0.500(5)\pi$, $V_{s,x} = V_{s,y} = 7.0(2)E_{r,s}$ and $V_{l,x} = V_{l,y} = 20.0(6)E_{r,l}$. The data are the average of 14 measurements for the point at $\varphi_x = 0$ and 7 measurements for all others; the error is the error of the mean. The dashed line shows the response of an ideal system; the solid line includes corrections for the finite pumping efficiency along x and for the creation of doubly occupied plaquettes and band excitations along y . Both curves are shifted by a constant offset $\mathcal{I}_0 = 0.002$ (see Methods). For simplicity, the theoretical curves assume a homogeneous Berry curvature $\Omega^x = \nu_1^x a_x/(2\pi)$, neglecting the variation in Ω^x during a pump cycle. **b**, The response of an infinite system can be reconstructed with a small cloud of atoms by repeating the measurement from **a** for different values of $\varphi_y^{(0)}$. A single measurement probes the response locally at the position of the cloud (grey frames on the left). Changing $\varphi_y^{(0)}$ is

An example measurement of $\mathcal{I}_y(\varphi_x)$ is shown in Fig. 3a. The measured nonlinear response is smaller than expected for an ideal system, owing to the appearance of doubly occupied plaquettes and band excitations along y during the pumping and to a finite pumping efficiency along x (see Methods). Taking these imperfections into account, we find excellent agreement between the experimental data and the expected imbalance (Fig. 3a). By performing a linear fit to the differential double-well imbalance $\mathcal{I}_y(\varphi_x) - \mathcal{I}_y(-\varphi_x)$, we extract the change in the population imbalance during one cycle, $\delta\mathcal{I}_y = \mathcal{I}_y(\varphi_x = 2\pi) - \mathcal{I}_y(\varphi_x = 0)$ (see Methods). For a homogeneously populated band, this slope is determined by $\sqrt{2}$ and thus characterizes the transport properties of the system.

To reconstruct the quantized response of an infinite system and thereby obtain ν_2 , we repeat the measurement of $\mathcal{I}_y(\varphi_x)$ for different $\varphi_y^{(0)}$ starting from the same initial position. This is equivalent to using the small cloud of atoms as a local probe at different positions along x for fixed $\varphi_y^{(0)}$ (Fig. 3b). To demonstrate the quantization of the nonlinear response, we determine the second Chern number of the lowest subband by averaging $\delta\mathcal{I}_y$ over $\varphi_y^{(0)} \in [0, 2\pi)$. For symmetry reasons, it is sufficient to restrict $\varphi_y^{(0)}$ to $[0, \pi)$ for $d_l = 2d_s$ (see Methods). In this interval, the nonlinear response has large contributions only in the vicinity of $\varphi_y^{(0)} = \pi/2$. For the range of data shown in Fig. 3c, this process gives $\nu_2^{\text{exp}} = 0.8(2)$, with the error resulting from the fit and the uncertainty in θ . By taking the above-mentioned experimental imperfections into account we isolate the contribution from the lowest subband $\delta\mathcal{I}_y^{\text{gs}}$ (see Methods). The experimentally determined slope of the nonlinear response for ground-state atoms agrees very well with the slope expected in an ideal system (Fig. 3c). To determine ν_2^{exp} , the ideal slope is fitted to the measured one by scaling it with a global amplitude, $(\nu_2^{\text{exp}}/\nu_2)\delta\mathcal{I}_y^{\text{gs}}(\varphi_y^{(0)})$. This yields $\nu_2^{\text{exp}} = 1.07(8)$, in agreement with the expected value of $\nu_2 = +1$. The error in here additionally takes into account the uncertainties in the lattice depths.

In the 4D quantum Hall system, the defining feature of the nonlinear response is its linear dependence on the magnetic perturbation. The same scaling is thus expected for the 2D charge pump with respect to θ .

equivalent to sampling a different position in the lattice (magnified frames on the right). Note that the tilt of the long y lattice (indicated by the red solid line, as in Fig. 1c) is greatly exaggerated compared to the angle used in the experiment. **c**, Change in the double-well imbalance per cycle for the lowest band ($\delta\mathcal{I}_y^{\text{gs}}$) as a function of $\varphi_y^{(0)}$. $\delta\mathcal{I}_y^{\text{gs}}$ is determined by the integrated Berry curvature $\overline{\Omega}(\varphi_y^{(0)})$ and so exhibits a pronounced peak around $\varphi_y^{(0)} = \pi/2$ (see Fig. 1e and Methods). The slope $\delta\mathcal{I}_y^{\text{gs}}$ is extracted from a fit to the measured imbalance $\mathcal{I}_y(\varphi_x)$ (see Methods) and the solid line is the theoretically expected slope. Error bars show the fit error and the blue-shaded region indicates the uncertainty of the theoretical curve that results from the errors in θ and the lattice depths. The insets show two additional examples of individual measurements of $\mathcal{I}_y(\varphi_x)$ (for the values of $\varphi_y^{(0)}$ indicated by the grey shading), as in **a**.

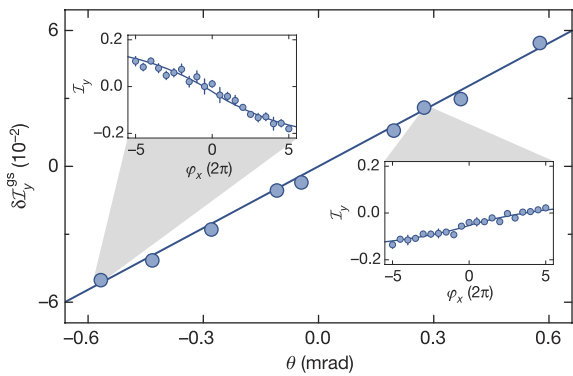


Figure 4 | Scaling of the 4D-like response with the tilt angle θ . The linear dependence on θ reveals the nonlinear character of the response, demonstrating that it is induced by two independent perturbations, $\partial\varphi_x/\partial t$ and θ . The slope $\delta\mathcal{I}_y^{\text{gs}}$ is determined as a function of θ at $\varphi_y^{(0)} = 0.500(5)\pi$ by measuring the double-well imbalance when pumping along x , as described in Fig. 3 and using the same lattice depths. The solid line shows the slope that is expected for an ideal system. The fit errors for $\delta\mathcal{I}_y^{\text{gs}}$ are smaller than the size of the data points and the insets show two examples of the measurement of $\mathcal{I}_y(\varphi_x)$ (for the values of θ indicated by the grey shading), as in Fig. 3a.

We verify this by measuring the peak slope $\delta\mathcal{I}_y^{\text{gs}}$ at $\varphi_y^{(0)} = \pi/2$ as a function of θ (Fig. 4). Doing so also provides another way of obtaining the second Chern number, by determining the slope of $\delta\mathcal{I}_y^{\text{gs}}(\theta)$ (see Methods). This linear fit gives $\nu_2^{\text{exp}} = 1.01(8)$, where the error is determined as described above. Furthermore, we confirm that the peak slope at fixed θ scales with the depth of the short y lattice $V_{s,y}$ as expected (Extended Data Fig. 1, Methods). In particular, the direction of the nonlinear response is independent of $V_{s,y}$, indicating its robustness against perturbations of the system.

In conclusion, we present an observation of a dynamical 4D quantum Hall effect, opening up a route to studying higher-dimensional quantum Hall physics experimentally. Extending our work, additional density-type nonlinear responses that are implied by the intrinsic 4D symmetry of a 2D charge pump can be measured⁶. By adding a spin-dependent Yang–Mills gauge field, a dynamical version of the time-reversal-symmetric 4D quantum Hall effect, which exhibits a ground state with $\text{SO}(5)$ symmetry, could be realized⁶. Including interactions may yield intriguing fractional phases that originate in the 4D fractional quantum Hall effect⁴, similarly to previous proposals for 1D charge pumps²⁸, and might enable the study of open questions in the context of Floquet engineering¹⁵. Going beyond the limit of weak perturbations, quantized electric quadrupole moments could be observed in spatially frustrated systems with $\theta = \pi/4$ (ref. 29). Furthermore, a quantum Hall system with four extended dimensions might be realized with cold atoms²⁰ using recently demonstrated techniques for creating synthetic dimensions^{18,19}. In finite systems, this would permit the observation of boundary phenomena such as isolated Weyl points³⁰. Ultimately, the ability to experimentally realize 4D quantum Hall systems could provide insight into lattice quantum chromodynamics models based on the Yang–Mills theory⁷, and even quantum gravity⁴.

We note that, simultaneously with this work, complementary results on topological edge states in 2D photonic pumps have been obtained³¹.

Online Content Methods, along with any additional Extended Data display items and Source Data, are available in the online version of the paper; references unique to these sections appear only in the online paper.

Received 23 May; accepted 31 October 2017.

1. Klitzing, K. v., Dorda, G. & Pepper, M. New method for high-accuracy determination of the fine-structure constant based on quantized Hall resistance. *Phys. Rev. Lett.* **45**, 494–497 (1980).
2. Thouless, D. J., Kohmoto, M., Nightingale, M. P. & den Nijs, M. Quantized Hall conductance in a two-dimensional periodic potential. *Phys. Rev. Lett.* **49**, 405–408 (1982).

3. Fröhlich, J. & Pedrini, B. in *Mathematical Physics 2000* (eds Fokas, A. et al.) 9–47 (Imperial College Press, 2000).
4. Zhang, S.-C. & Hu, J. A four-dimensional generalization of the quantum Hall effect. *Science* **294**, 823–828 (2001).
5. Thouless, D. J. Quantization of particle transport. *Phys. Rev. B* **27**, 6083–6087 (1983).
6. Kraus, Y. E., Ringel, Z. & Zilberberg, O. Four-dimensional quantum Hall effect in a two-dimensional quasicrystal. *Phys. Rev. Lett.* **111**, 226401 (2013).
7. Yang, C. N. & Mills, R. L. Conservation of isotopic spin and isotopic gauge invariance. *Phys. Rev.* **96**, 191–195 (1954).
8. Qi, X.-L. & Zhang, S.-C. Topological insulators and superconductors. *Rev. Mod. Phys.* **83**, 1057–1110 (2011).
9. Nayak, C., Simon, S. H., Stern, A., Freedman, M. & Das Sarma, S. Non-Abelian anyons and topological quantum computation. *Rev. Mod. Phys.* **80**, 1083–1159 (2008).
10. Laughlin, R. B. Quantized Hall conductivity in two dimensions. *Phys. Rev. B* **23**, 5632–5633 (1981).
11. Lu, L. et al. Experimental observation of Weyl points. *Science* **349**, 622–624 (2015).
12. Xu, S.-Y. et al. Discovery of a Weyl fermion semimetal and topological Fermi arcs. *Science* **349**, 613–617 (2015).
13. Hsieh, D. et al. A topological Dirac insulator in a quantum spin Hall phase. *Nature* **452**, 970–974 (2008).
14. Qi, X.-L., Hughes, T. L. & Zhang, S.-C. Topological field theory of time-reversal invariant insulators. *Phys. Rev. B* **78**, 195424 (2008).
15. Goldman, N., Budich, J. C. & Zoller, P. Topological quantum matter with ultracold gases in optical lattices. *Nat. Phys.* **12**, 639–645 (2016).
16. Lu, L., Joannopoulos, J. D. & Soljacic, M. Topological photonics. *Nat. Photon.* **8**, 821–829 (2014).
17. Sugawa, S., Salces-Carcoba, F., Perry, A. R., Yue, Y. & Spielman, I. B. Observation of a non-abelian Yang monopole: from new Chern numbers to a topological transition. Preprint at <http://arxiv.org/abs/1610.06228> (2016).
18. Mancini, M. et al. Observation of chiral edge states with neutral fermions in synthetic Hall ribbons. *Science* **349**, 1510–1513 (2015).
19. Stuhl, B. K., Lu, H.-I., Ayccock, L. M., Genkina, D. & Spielman, I. B. Visualizing edge states with an atomic Bose gas in the quantum Hall regime. *Science* **349**, 1514–1518 (2015).
20. Price, H. M., Zilberberg, O., Ozawa, T., Carusotto, I. & Goldman, N. Four-dimensional quantum Hall effect with ultracold atoms. *Phys. Rev. Lett.* **115**, 195303 (2015).
21. Price, H. M., Zilberberg, O., Ozawa, T., Carusotto, I. & Goldman, N. Measurement of Chern numbers through center-of-mass responses. *Phys. Rev. B* **93**, 245113 (2016).
22. Kraus, Y. E. & Zilberberg, O. Topological equivalence between the Fibonacci quasicrystal and the Harper model. *Phys. Rev. Lett.* **109**, 116404 (2012).
23. Switkes, M., Marcus, C. M., Campman, K. & Gossard, A. C. An adiabatic quantum electron pump. *Science* **283**, 1905–1908 (1999).
24. Kraus, Y. E., Lahini, Y., Ringel, Z., Verbin, M. & Zilberberg, O. Topological states and adiabatic pumping in quasicrystals. *Phys. Rev. Lett.* **109**, 106402 (2012).
25. Lohse, M., Schweizer, C., Zilberberg, O., Aidelsburger, M. & Bloch, I. A Thouless quantum pump with ultracold bosonic atoms in an optical superlattice. *Nat. Phys.* **12**, 350–354 (2016).
26. Nakajima, S. et al. Topological Thouless pumping of ultracold fermions. *Nat. Phys.* **12**, 296–300 (2016).
27. Rice, M. J. & Mele, E. J. Elementary excitations of a linearly conjugated diatomic polymer. *Phys. Rev. Lett.* **49**, 1455–1459 (1982).
28. Zhu, S.-L., Wang, Z.-D., Chan, Y.-H. & Duan, L.-M. Topological Bose–Mott insulators in a one-dimensional optical superlattice. *Phys. Rev. Lett.* **110**, 075303 (2013).
29. Benalcazar, W. A., Bernevig, B. A. & Hughes, T. L. Quantized electric multipole insulators. *Science* **357**, 61–66 (2017).
30. Hosur, P. & Qi, X. Recent developments in transport phenomena in Weyl semimetals. *C. R. Phys.* **14**, 857–870 (2013).
31. Zilberberg, O. et al. Photonic topological boundary pumping as a probe of 4D quantum Hall physics. *Nature* **553**, <https://doi.org/10.1038/nature25011> (2018).

Acknowledgements We acknowledge discussions with M. Aidelsburger and I. Carusotto. This work was funded by the European Commission (UQUAM, SIQS), the Deutsche Forschungsgemeinschaft (DIP, FOR2414) and the Nanosystems Initiative Munich. M.L. was additionally supported by the Elitenetzwerk Bayern (EXQM), H.M.P. by the European Commission (FET Proactive, grant no. 640800 ‘AQuS’), and Marie Skłodowska–Curie Action, grant no. 656093 ‘SynOptic’) and the Autonomous Province of Trento (SiQuero), and O.Z. by the Swiss National Science Foundation.

Author Contributions M.L. and C.S. performed the experiment and data analysis. O.Z. proposed the experiment. All authors contributed to the theoretical analysis and to writing the paper. I.B. supervised the project.

Author Information Reprints and permissions information is available at www.nature.com/reprints. The authors declare no competing financial interests. Readers are welcome to comment on the online version of the paper. Publisher’s note: Springer Nature remains neutral with regard to jurisdictional claims in published maps and institutional affiliations. Correspondence and requests for materials should be addressed to I.B. (immanuel.bloch@physik.uni-muenchen.de).

METHODS

Hall response of the 4D quantum Hall system. Assuming perfect adiabaticity, the Hall response of the 4D system shown in Fig. 1a, b can be evaluated from the semi-classical equations of motion for a wave packet centred at position \mathbf{r} and quasi-momentum \mathbf{k} (ref. 32)

$$\dot{r}^\mu = \frac{1}{\hbar} \frac{\partial \mathcal{E}(\mathbf{k})}{\partial k_\mu} + \dot{k}_\nu \Omega^{\nu\mu}(\mathbf{k})$$

$$\hbar \dot{k}_\mu = qE_\mu + q\dot{r}^\nu B_{\mu\nu}$$

Here, $\mathcal{E}(\mathbf{k})$ is the energy of the respective eigenstate at \mathbf{k} , q is the charge of the particle and Einstein notation is used for the spatial indices $\mu, \nu \in \{w, x, y, z\}$. The orientation of the axes in Fig. 1a, b is chosen such that the 4D Levi-Civita symbol is $\varepsilon_{wxyz} = +1$. The velocity of the wave packet $\mathbf{v} = \dot{\mathbf{r}}$ has two contributions: the group velocity, which arises from the dispersion of the band, and the anomalous velocity, which is due to the non-zero Berry curvature

$$\Omega^{\nu\mu}(\mathbf{k}) = i(\langle \partial_{k_\nu} u | \partial_{k_\mu} u \rangle - \langle \partial_{k_\mu} u | \partial_{k_\nu} u \rangle)$$

For a filled or homogeneously populated band, the group velocity term vanishes and with $\mathbf{E} = E_z \mathbf{e}_z$ and $\mathbf{B} = \mathbf{0}$ the linear Hall response is given by the COM velocity

$$\mathbf{v}_{\text{COM}}^{(0)} = \frac{q}{h} A_M^{\text{zx}} E_z \nu_1^{\text{zx}} \mathbf{e}_x$$

where A_M^{zx} denotes the size of the magnetic unit cell in the x - z plane and

$$\nu_1^{\text{zx}} = \frac{1}{2\pi} \oint_{\text{BZ}} \Omega^{\text{zx}} d^2k$$

denotes the first Chern number of the 2D quantum Hall system in the x - z plane. The integration is performed over the 2D Brillouin zone (BZ) spanned by k_x and k_z .

Adding the perturbing magnetic field B_{xw} generates a Lorentz force that acts on the moving cloud²⁰, $\hbar \dot{\mathbf{k}} = qE_z \mathbf{e}_z - qv_x^{(0)} B_{xw} \mathbf{e}_w$. (This additional force can alternatively be interpreted as arising from a Hall voltage in the w direction that is created by the current along x in the presence of B_{xw} .) This force in turn induces an additional anomalous velocity along y , giving rise to the nonlinear Hall response. The resulting average velocity is then

$$\mathbf{v}_{\text{COM}} = \frac{q}{h} A_M^{\text{zx}} E_z \nu_1^{\text{zx}} \mathbf{e}_x - \left(\frac{q}{h} \right)^2 A_M E_z B_{xw} \nu_2 \mathbf{e}_y$$

with A_M the size of the 4D magnetic unit cell. The second Chern number is given by

$$\nu_2 = \frac{1}{4\pi^2} \oint_{\text{BZ}} \Omega^{xw} \Omega^{zy} + \Omega^{xy} \Omega^{wz} + \Omega^{zx} \Omega^{wy} d^4k$$

where BZ denotes the 4D Brillouin zone.

Tight-binding Hamiltonian of the 2D superlattice. In the tight-binding limit, the motion of non-interacting atoms in a 2D superlattice is captured by the following Hamiltonian

$$\hat{H}_{2\text{D}}(\varphi_x, \varphi_y) =$$

$$- \sum_{m_x, m_y} \left[J_x(\varphi_x) + \delta J_x^{m_x}(\varphi_x) \right] \hat{a}_{m_x+1, m_y}^\dagger \hat{a}_{m_x, m_y} + \text{h.c.}$$

$$- \sum_{m_x, m_y} \left[J_y(\varphi_y) + \delta J_y^{m_y}(\varphi_y) \right] \hat{a}_{m_x, m_y+1}^\dagger \hat{a}_{m_x, m_y} + \text{h.c.} \quad (1)$$

$$+ \sum_{m_x, m_y} \left[\Delta_x^{m_x}(\varphi_x) + \Delta_y^{m_y}(\varphi_y) \right] \hat{a}_{m_x, m_y}^\dagger \hat{a}_{m_x, m_y}$$

Here, $\hat{a}_{m_x, m_y}^\dagger$ (\hat{a}_{m_x, m_y}) is the creation (annihilation) operator acting on the (m_x, m_y) th site in the x - y plane. The first (second) term describes the hopping between neighbouring sites along the x axis (y axis), with tunnelling matrix elements $J_\mu + \delta J_\mu^{m_\mu}$, with $\mu \in \{x, y\}$. The last term contains the on-site potential of each lattice site, $\Delta_x^{m_x} + \Delta_y^{m_y}$. In the presence of the long lattices, the tunnel couplings and on-site energies are modulated periodically by $\delta J_\mu^{m_\mu}$ and $\Delta_x^{m_x} + \Delta_y^{m_y}$, respectively. Both modulations depend on the respective superlattice phases φ_μ .

For the lattice configuration used in the experiment, where $d_{1\mu} = 2d_{s,\mu}$, these modulations can be expressed as $(-1)^{m_\mu} \delta J_\mu^{m_\mu}/2$ and $(-1)^{m_\mu} \Delta_\mu/2$, and equation (1) reduces to the 2D Rice-Mele Hamiltonian²⁷

$$\hat{H}_{2\text{D}}(\varphi_x, \varphi_y) =$$

$$- \sum_{m_x, m_y} \left[J_x(\varphi_x) + (-1)^{m_x} \delta J_x(\varphi_x)/2 \right] \hat{a}_{m_x+1, m_y}^\dagger \hat{a}_{m_x, m_y} + \text{h.c.}$$

$$- \sum_{m_x, m_y} \left[J_y(\varphi_y) + (-1)^{m_y} \delta J_y(\varphi_y)/2 \right] \hat{a}_{m_x, m_y+1}^\dagger \hat{a}_{m_x, m_y} + \text{h.c.}$$

$$+ \sum_{m_x, m_y} \frac{1}{2} \left[(-1)^{m_x} \Delta_x(\varphi_x) + (-1)^{m_y} \Delta_y(\varphi_y) \right] \hat{a}_{m_x, m_y}^\dagger \hat{a}_{m_x, m_y}$$

Mapping a 2D topological charge pump to a 4D quantum Hall system. The Hamiltonian of a 2D topological charge pump for a given set of parameters $\{\varphi_x, \varphi_y\}$, $\hat{H}_{2\text{D}}(\varphi_x, \varphi_y)$, can be interpreted as a Fourier component of a higher-dimensional quantum Hall system. Using the approach of dimensional extension^{6,22}, a 2D charge pump can be mapped onto a 4D quantum Hall system, the Fourier components of which are sampled sequentially during a pump cycle. This is demonstrated in the following for the deep tight-binding limit $V_{s,\mu} \gg V_{1,\mu}^2/(4E_{r,s})$, $\mu \in \{x, y\}$, in which the corresponding 4D system consists of two 2D Harper-Hofstadter-Hatsugai models³³⁻³⁶ in the x - z and y - w planes. A similar analogy can be made in the opposite limit of vanishingly short lattices, $V_{s,x} \rightarrow 0$ and $V_{s,y} \rightarrow 0$. In this case, each axis of the 2D lattice maps onto the Landau levels of a free particle in an external magnetic field in two dimensions²⁵. For the lowest band, these two limiting cases are topologically equivalent; that is, they are connected by a smooth crossover without closing the gap to the first excited band. The topological invariants that govern the linear and nonlinear response are thus independent of the depth of the short lattices.

In the deep tight-binding regime, J_x and J_y become independent of the superlattice phases and the modulations can be approximated as³⁷

$$\delta J_x^{m_x}(\varphi_x) = \frac{\delta J_x^{(0)}}{2} \cos[\tilde{\Phi}_{xz}(m_x + 1/2) - \varphi_x]$$

$$\delta J_y^{m_y}(\varphi_y) = \frac{\delta J_y^{(0)}}{2} \cos[\tilde{\Phi}_{yw}(m_y + 1/2) - \varphi_y]$$

$$\Delta_x^{m_x}(\varphi_x) = -\frac{\Delta_x^{(0)}}{2} \cos(\tilde{\Phi}_{xz} m_x - \varphi_x)$$

$$\Delta_y^{m_y}(\varphi_y) = -\frac{\Delta_y^{(0)}}{2} \cos(\tilde{\Phi}_{yw} m_y - \varphi_y)$$

with $\tilde{\Phi}_{xz} = 2\pi d_{s,x}/d_{1,x}$ and $\tilde{\Phi}_{yw} = 2\pi d_{s,y}/d_{1,y}$, $\delta J_\mu^{(0)}$ and $\Delta_\mu^{(0)}$ denote the modulation amplitudes, which are determined by the lattice depths. In this case, $\hat{H}_{2\text{D}}$ is equivalent to the generalized 2D Harper model³³, which describes the Fourier components of a 4D lattice model with two uniform magnetic fields in orthogonal subspaces. The 4D parent Hamiltonian is obtained via an inverse Fourier transform⁶

$$\hat{H}_{4\text{D}} = \frac{1}{4\pi^2} \int_0^{2\pi} \int_0^{2\pi} \hat{H}_{2\text{D}}(\varphi_x, \varphi_y) d\varphi_x d\varphi_y^{(0)}$$

with

$$\hat{a}_{m_x, m_y}^\dagger = \sum_{m_z, m_w} e^{i(\varphi_x m_z + \varphi_y^{(0)} m_w)} \hat{a}_m^\dagger$$

$$\hat{a}_{m_x, m_y} = \sum_{m_z, m_w} e^{-i(\varphi_x m_z + \varphi_y^{(0)} m_w)} \hat{a}_m$$

and where $\mathbf{m} = \{m_x, m_y, m_z, m_w\}$ indicates the position in the 4D lattice. This yields

$$\hat{H}_{4\text{D}} = \hat{H}_{xz} + \hat{H}_{yw} + \hat{H}_{\delta J}$$

The first term (\hat{H}_{xz}) describes a 2D Harper-Hofstadter model³³⁻³⁵ in the x - z plane with a uniform magnetic flux per unit cell, $\tilde{\Phi}_{xz} = \Phi_0 \tilde{\Phi}_{xz}/(2\pi) = (d_{s,x}/d_{1,x}) \Phi_0$, with Φ_0 denoting the magnetic flux quantum

$$\hat{H}_{xz} = - \sum_{\mathbf{m}} J_x \hat{a}_{\mathbf{m}+\mathbf{e}_x}^\dagger \hat{a}_{\mathbf{m}} + \text{h.c.}$$

$$- \sum_{\mathbf{m}} \frac{\Delta_x^{(0)}}{4} e^{i\tilde{\Phi}_{xz} m_x} \hat{a}_{\mathbf{m}+\mathbf{e}_z}^\dagger \hat{a}_{\mathbf{m}} + \text{h.c.}$$

Correspondingly, the second term (\hat{H}_{yw}) is an independent 2D Harper-Hofstadter model in the y - w plane with $\tilde{\Phi}_{yw} = (d_{s,y}/d_{1,y}) \Phi_0$. Owing to the positional dependence

of the transverse superlattice phase φ_y , this term also contains the magnetic perturbation, that is, a weak homogeneous magnetic field in the x - w plane

$$\hat{H}_{yw} = - \sum_m J_y \hat{a}_{m+e_y}^\dagger \hat{a}_m + \text{h.c.} \\ - \sum_m \frac{\Delta_y^{(0)}}{4} e^{i(\tilde{\Phi}_{ym} m_y + \tilde{\Phi}_{xw} m_x)} \hat{a}_{m+e_w}^\dagger \hat{a}_m + \text{h.c.}$$

with $\tilde{\Phi}_{xw} = -2\pi\theta d_{s,x}/d_{l,y}$. The strength of the perturbing magnetic field is then

$$B_{xw} = - \frac{\tilde{\Phi}_0}{d_{s,w} d_{l,y}} \theta$$

where $d_{s,w}$ is the lattice spacing along w . For $\delta J_\mu^{(0)} \neq 0$, the third contribution ($\hat{H}_{\delta J}$) leads to the appearance of additional next-nearest-neighbour tunnel coupling elements in the x - z and y - w planes, with amplitudes of $\delta J_x^{(0)}/4$ and $\delta J_y^{(0)}/4$, respectively. The individual 2D models without the magnetic perturbation B_{xw} then correspond to the Harper–Hofstadter–Hatsugai model³⁶ with a uniform magnetic flux $\tilde{\Phi}_{xz}$ and $\tilde{\Phi}_{yw}$, the same flux as for $\delta J_\mu^{(0)} = 0$.

Transport properties of a 2D topological charge pump. When the pump parameter φ_x is changed slowly, a particle that is initially in an eigenstate $|u(k_x, \varphi_x(t=0), k_y, \varphi_y)\rangle$ of the 2D superlattice Hamiltonian \hat{H}_{2D} (equation (1)) will adiabatically follow the corresponding instantaneous eigenstate $|u(k_x, \varphi_x(t), k_y, \varphi_y)\rangle$. In absence of a tilt ($\theta=0$), the particle acquires an anomalous velocity $\Omega^x \partial_t \varphi_x \mathbf{e}_x$ during this evolution, analogously to the linear Hall response in a quantum Hall system. In this case, the Berry curvature Ω^x is defined in a 4D generalized Brillouin zone ($k_x, \varphi_x, k_y, \varphi_y$)

$$\Omega^x(k_x, \varphi_x, k_y, \varphi_y) = i(\langle \partial_{\varphi_x} u | \partial_{k_x} u \rangle - \langle \partial_{k_x} u | \partial_{\varphi_x} u \rangle)$$

For a homogeneously populated band, the COM displacement along x during one cycle, obtained by integrating the average anomalous velocity over one period, can be expressed as an integral of the Berry curvature over the 2D generalized Brillouin zone spanned by k_x and φ_x . It is therefore determined by the first Chern number of the pump

$$\nu_1^x = \frac{1}{2\pi} \oint \Omega^x dk_x d\varphi_x$$

When a tilt is present ($\theta \neq 0$), this motion along x leads to a change in φ_y . This induces an additional anomalous velocity in the y direction, giving rise to the nonlinear response. Neglecting the contribution from the group velocity (which averages to zero for a homogeneously populated band), we obtain for a given eigenstate

$$v_y(k_x, \varphi_x, k_y, \varphi_y) = \Omega^y \partial_t \varphi_y = \frac{2\pi}{d_{l,y}} \theta \Omega^x \Omega^y \partial_t \varphi_x \quad (2)$$

The distribution of $\Omega^x \Omega^y$ in the 4D generalized Brillouin zone is shown in Fig. 1e for the lattice parameters used for the measurements in Figs 3 and 4. It exhibits pronounced peaks around $\varphi_x \in \{\pi/2, 3\pi/2\}$ and $\varphi_y \in \{\pi/2, 3\pi/2\}$. For $d_l = 2d_s$, $\Omega^x \Omega^y$ is π -periodic in both φ_x and φ_y because the corresponding eigenstates are related by a gauge transformation, owing to the translational symmetry of the superlattice potential³⁸.

For a small cloud that homogeneously populates a single band, as in the experiment, the variation in $\Omega^x \Omega^y$ over the size of the cloud along x (L_x) due to the position dependence of φ_y is negligible for $L_x \ll d_{l,y}/\theta$. The average velocity for the nonlinear response can then be calculated by averaging equation (2) over both quasi-momenta k_x and k_y . The COM displacement after a complete cycle can be determined by integrating the velocity over one period. We can thus express the change in the COM position per cycle as

$$\delta y_{\text{COM}} = \frac{1}{2\pi} \oint \frac{\Omega^x \Omega^y dk_x dk_y d\varphi_x}{\bar{\Omega}(\varphi_y)} \frac{a_x}{d_{l,y}} a_y \quad (3)$$

If the number of pump cycles is small, then the change in φ_y as a result of the linear pumping response can be neglected and the nonlinear displacement per cycle is very well approximated by $\delta y_{\text{COM}} \approx \bar{\Omega}(\varphi_y^{(0)}) \theta a_x a_y / d_{l,y}$.

The response of a large system with $L_x \gg d_{l,y}/\theta$ can be obtained by averaging equation (3) over $\varphi_y(x) \in [0, 2\pi]$, yielding

$$\delta y_{\text{COM}} = \frac{1}{2\pi} \oint \bar{\Omega}(\varphi_y) \theta \frac{a_x}{d_{l,y}} a_y d\varphi_y = \nu_2 \theta \frac{a_x}{d_{l,y}} a_y$$

where the second Chern number ν_2 is calculated by integrating $\Omega^x \Omega^y$ over the entire 4D generalized Brillouin zone

$$\nu_2 = \frac{1}{4\pi^2} \oint_{\text{BZ}} \Omega^x \Omega^y dk_x dk_y d\varphi_x d\varphi_y$$

Note that to probe the intrinsic transport properties of the unperturbed system, both fields that generate the response have to be small perturbations such that the evolution remains adiabatic and the energy gap to the excited subbands remains open, which protects the topological invariants. Nonetheless, going beyond this limit can result in additional exciting phenomena. For example, a configuration with $\theta = \pi/4$ can lead to spatial frustration and the resulting model might enable the observation of quantized electric quadrupole moments similar to those proposed previously²⁹.

Pump path. Varying the pump parameter φ_x periodically modulates the tight-binding parameters $\delta J_x(\varphi_x)$ and $\Delta_x(\varphi_x)$ that describe the superlattice along x (equation (1)). For $d_l = 2d_s$, the modulation of δJ_x and Δ_x is out of phase and the system therefore evolves along a closed trajectory in the δJ_x - Δ_x parameter space (Extended Data Fig. 2a). This pump path encircles the degeneracy point ($\delta J_x = 0, \Delta_x = 0$), at which the two lowest subbands of the Rice–Mele model touch. This singularity can be interpreted as the source of the non-zero Berry curvature Ω^x in the generalized Brillouin zone, which gives rise to the linear pumping response. All pump paths that encircle the degeneracy can be continuously transformed into one another without closing the gap to the first excited subband and are thus topologically equivalent with respect to the linear response; that is, the value of ν_1^x does not change.

Similarly, the tight-binding parameters δJ_y and Δ_y depend on the phase of the transverse superlattice φ_y . For a large cloud, all possible values of φ_y , and thus δJ_y and Δ_y , are sampled simultaneously (Extended Data Fig. 2b). During a pump cycle, the system therefore traces out a closed surface in the 4D parameter space of $\delta J_x, \Delta_x, \delta J_y$ and Δ_y (Extended Data Fig. 2c). In this parameter space, the two lowest subbands touch in the two planes ($\delta J_x = 0, \Delta_x = 0$) and ($\delta J_y = 0, \Delta_y = 0$), which intersect at a single point at the origin (Extended Data Fig. 2d). Analogously to the linear response, this degeneracy generates the non-zero Berry curvatures Ω^x and Ω^y , which cause the nonlinear motion in the y direction. Owing to the 4D character of the parameter space, the 4D pump path can enclose the degeneracy (Extended Data Fig. 2e). Whenever this is the case, the topology of the cycle does not change and the value of ν_2 remains the same.

To visualize the pump path in the 4D parameter space in Extended Data Fig. 2, we apply the following transformation

$$\begin{pmatrix} r_1 \\ r_2 \\ r_3 \\ r_4 \end{pmatrix} = \frac{1}{4} \begin{pmatrix} 1 & 1 & -1 & -1 \\ 1 & 1 & 1 & 1 \\ 1 & -1 & -1 & 1 \\ 1 & -1 & 1 & -1 \end{pmatrix} \begin{pmatrix} \delta J_x / \delta J_x^{(0)} \\ \Delta_x / \Delta_x^{(0)} \\ \delta J_y / \delta J_y^{(0)} \\ \Delta_y / \Delta_y^{(0)} \end{pmatrix} \quad (4)$$

where the tight-binding parameters are normalized by their respective maximum values. The degeneracy planes are then given by $r_1 = -r_2, r_3 = -r_4$ and $r_1 = r_2, r_3 = r_4$, respectively; that is, they become perpendicular planes in (r_1, r_2, r_3) space.

Lattice configuration. All experiments were performed in a mutually orthogonal retro-reflected 3D optical lattice consisting of superlattices along x and y and a simple lattice in the z direction. Each superlattice is created by superimposing two standing waves: a short lattice with wavelength $\lambda_s = 767$ nm and a long lattice with $\lambda_l = 2\lambda_s$. The vertical lattice along z is formed by a standing wave with $\lambda_z = 844$ nm.

Initial state preparation for band-mapping measurements. For all sequences, a quarter-filled Mott insulator consisting of about 5,000 ⁸⁷Rb atoms was prepared with one atom localized in the ground state of each unit cell, creating a uniform occupation of the lowest subband in the 2D superlattice. To this end, a Bose–Einstein condensate was loaded from a crossed dipole trap into the lattice by first ramping up the blue-detuned short lattices along x and y to $3.0(1)E_{r,s}$ over 50 ms to lower the initial density of the cloud of atoms. These lattices were then switched off again within 50 ms, while the vertical lattice and both long lattices were increased to $30(1)E_{r,z}$ and $30(1)E_{r,l}$, respectively, with $\varphi_x = 0.000(5)\pi$ and $\varphi_y = \varphi_y^{(0)}$. Subsequently, doubly occupied lattice sites were converted to singly occupied ones (see below), creating a Mott insulator with unit filling and a negligible fraction of doublons. Each lattice site was then split into a four-site plaquette by ramping up the short lattices along x and y to their final depth of $7.0(2)E_{r,s}$ and decreasing the long lattices to $20.0(6)E_{r,l}$ over 5 ms.

Removing doubly occupied sites. After preparing the Mott insulator with unit filling in the long lattices, sites containing two atoms were converted to singly occupied ones using microwave-dressed spin-changing collisions and a

resonant optical push-out pulse^{39,40}. For this, the lattice depths are increased to $V_{s,x} = 70(2)E_{r,s}$, $V_{l,x} = 30(1)E_{r,l}$, $V_{l,y} = 70(2)E_{r,l}$ and $V_z = 100(3)E_{r,z}$ over 5 ms to maximize the on-site interaction energy. The atoms, which were initially in the ($F=1$, $m_F=-1$) hyperfine state, were converted to ($F=1$, $m_F=0$) by using an adiabatic radio-frequency transfer. Here, F denotes the total angular momentum of the atoms. By ramping a magnetic offset field in the presence of a microwave field, we performed a Landau-Zener sweep that adiabatically converted pairs of $m_F=0$ atoms on the same lattice site to an $m_F=+1$ and an $m_F=-1$ atom via coherent spin-changing collisions. The $m_F=-1$ atoms were subsequently removed via an adiabatic microwave transfer to ($F=2$, $m_F=-2$), which was followed by a resonant optical pulse after lowering the lattices to $V_{s,x}=0E_{r,s}$, $V_{l,x}=30(1)E_{r,l}$, $V_{l,y}=40(1)E_{r,l}$ and $V_z=40(1)E_{r,z}$.

Sequence for pumping. The superlattice phase can be controlled by slightly changing the frequency of the lasers used for generating the long lattices and thereby moving the relative position between the short and long lattices at the position of the atoms. The pumping along x is performed by slowly changing φ_x , starting from the staggered configuration at $\varphi_x = 0.000(5)\pi$, in which the energy difference between neighbouring sites ($|\Delta_x|$) is largest and the tunnel couplings are equal ($\delta J_x = 0$). To minimize non-adiabatic transitions to higher bands, each pump cycle consists of three S-shaped ramps: $\varphi_x \in [0, 0.5\pi]$, $[0.5\pi, 1.5\pi]$ and $[1.5\pi, 2\pi]$. This reduces the ramp speed in the vicinity of the symmetric double-well configuration ($\Delta_x=0$) at $\varphi_x = (l+1/2)\pi$, with $l \in \mathbb{Z}$, at which the gap to the first excited band is smallest. The duration of the $\pi/2$ ramps is 7 ms, and 14 ms for the ramp by π . Owing to the limited tuning range of a single laser, a second laser is required for implementing multiple pump cycles, which is set to a constant phase of $\varphi_x = 0.000(5)\pi$. At the end of each cycle, an instantaneous switch from the primary laser to the secondary one is made, and within 5 ms the frequency of the former is ramped back to its initial value, corresponding to an identical lattice configuration. After switching back to the first laser, the next cycle continues as described above. We checked experimentally that this handover between the two lasers does not create any measurable band excitations.

Measuring the *in situ* position. To determine the nonlinear COM displacement along y , a double-differential measurement was conducted to minimize the effect of shot-to-shot fluctuations of the atom position. To do this, the COM position is measured before (y_i) and after (y_f) the pumping and compared to a reference sequence ($y_i^{(0)}$, $y_f^{(0)}$). For the latter measurement, the pumping is performed with only the short lattice along y (at $V_{s,y} = 40(1)E_{r,s}$); there is therefore no nonlinear response. The initial position is obtained during the doublon removal sequence, where the atoms are initially prepared in the ($F=1$, $m_F=0$) hyperfine state and one atom from each doubly occupied site is transferred to ($F=2$, $m_F=-2$) using microwave-dressed spin-changing collisions (see above). In addition, we transfer 50% of the atoms on singly occupied sites to the $F=2$ manifold, by applying a microwave π pulse resonant on the ($F=1$, $m_F=0$) \rightarrow ($F=2$, $m_F=0$) transition. The $F=2$ atoms thus have the same density distribution as the remaining $F=1$ atoms and are imaged before the push-out pulse, which removes them from the lattice. The motion of the atoms due to the nonlinear response is then $\Delta y = (y_f - y_i) - (y_f^{(0)} - y_i^{(0)})$. The difference in the COM displacement along y between θ_1 and θ_2 is defined as $\Delta r_y = \Delta y(\theta_1) - \Delta y(\theta_2)$. For the x direction, it is obtained from $\Delta x = (x_f - x_i) - \delta \bar{x}$ directly without comparing it to the reference sequence. Here, $\delta \bar{x}$ is the average displacement of all data for a given angle, accounting for a small constant offset between the measured initial and final positions.

Relation between COM position and double-well imbalance. If there are no inter-double-well transitions along y , then the change in the double-well imbalance $\delta \mathcal{I}_y = \mathcal{I}_y(\varphi_x) - \mathcal{I}_y(\varphi_x=0)$ can be related directly to the COM motion along y . The COM position in the y direction is

$$y_{\text{COM}} = \frac{d_l}{N} \sum_{ij} [(j-1/4)N_{e,ij} + (j+1/4)N_{o,ij}]$$

where the sum is over all unit cells, $N_{e,ij}$ ($N_{o,ij}$) is the occupation of the even (odd) sites along y in the (i, j) th unit cell and N is the total number of atoms. Expressing this in terms of the total number of atoms on even and odd sites, $N_e = \sum_{ij} N_{e,ij}$ and $N_o = \sum_{ij} N_{o,ij}$, and assuming that there are no transitions between neighbouring unit cells along y (that is, $\sum_i (N_{e,ij} + N_{o,ij})$ remains constant), the change in the COM position can be written as $\delta y_{\text{COM}} = y_{\text{COM}}(\varphi_x) - y_{\text{COM}}(\varphi_x=0) = d_l \delta \mathcal{I}_y / 4$. Note that this derivation implicitly assumes that the COM of the maximally localized Wannier functions on the lattice sites along y is independent of φ_y , which is a valid approximation deep in the tight-binding regime; otherwise, the proportionality factor $d_l/2$ has to be replaced by the distance between the COM of the Wannier functions on the even and odd sites of a double well.

Direct determination of the second Chern number. To determine the second Chern number directly from the measured double-well imbalance $\mathcal{I}_y(\varphi_x)$, the

average change in the imbalance per cycle for the entire cloud $\delta \mathcal{I}_y(\varphi_y^{(0)})$ is obtained from a linear fit of the differential imbalance $\mathcal{I}_y(\varphi_x) - \mathcal{I}_y(-\varphi_x)$ for each value of $\varphi_y^{(0)}$. The influence of the excitations can be reduced by restricting the fitting region to a small number of pump cycles. The response of an infinite system is reconstructed by averaging $\delta \mathcal{I}_y(\varphi_y^{(0)})$ over $\varphi_y^{(0)}$ using linear interpolation between the data points. When taking into account all points with $\varphi_y/(2\pi) \leq 3$, this gives $\nu_2^{\text{exp}} = 0.84(17)$ for the data in Fig. 3. Note that the linear interpolation for the discrete sampling used in Fig. 3c leads to a systematic shift in ν_2^{exp} of +0.05. When correcting for the finite pumping efficiency along x (see below), which can be measured independently without prior knowledge about the system, we obtain $\nu_2^{\text{exp}} = 0.94(19)$.

Model for double-well imbalance including experimental imperfections. To isolate the nonlinear response of the lowest band from the band-mapping data, we use a simple model that takes into account band excitations and double occupation of plaquettes, and the experimental pumping efficiency of the linear response. The average double-well imbalance $\mathcal{I}_y(\varphi_x)$ can be written as

$$\mathcal{I}_y(\varphi_x) = n_{\text{gs}} \mathcal{I}_y^{\text{gs}}(\varphi_y) + n_{\text{exc}} \mathcal{I}_y^{\text{exc}}(\varphi_y) + n_2 \mathcal{I}_y^{2,\text{gs}}(\varphi_y)$$

where n_{gs} (n_{exc}) is the fraction of atoms on singly occupied plaquettes in the ground (first excited) state along y and n_2 is the fraction of atoms on doubly occupied plaquettes, which we assume to be in the ground state. These quantities can be determined experimentally at each point in the pumping sequence. $\mathcal{I}_y^{\text{gs}}$, $\mathcal{I}_y^{\text{exc}}$ and $\mathcal{I}_y^{2,\text{gs}}$ denote the imbalances of the corresponding states, which depend on the local phase of the y superlattice at the position of the cloud along x , $\varphi_y(x_{\text{COM}})$. The imbalance curves can be calculated theoretically using the respective double-well Hamiltonian (equations (5) or (6)) and can be obtained experimentally by studying the linear pumping response. The COM position in turn depends on the pump parameter φ_x and includes corrections for the finite pumping efficiency

$$x_{\text{COM}}(\varphi_x) = \text{sgn}(\varphi_x) \sum_{i=1}^{|\varphi_x|/\pi} (2\beta_0 \beta^i - \beta) d_s$$

for $\varphi_x/\pi \in \mathbb{Z}$. Here, $\beta_0 = 0.980(4)$ is the initial ground-state occupation along x and $\beta = 0.986(2)$ is the pumping efficiency, given by the fraction of atoms that remain in the lowest subband during each half of a pump cycle and are therefore transferred by one lattice site along x . The main contributions that limit the pumping efficiency are band excitations in the pumping direction and non-adiabatic transitions between neighbouring double wells induced by the external harmonic confinement. Although the local slope of the transverse response for doubly occupied plaquettes differs from that for single atoms, they exhibit the same quantized transport along x and y for the parameters used in the experiment when covering the entire 4D pump path.

Measuring band excitations. Band excitations in the y direction are measured by adiabatically ramping the superlattice phase $\varphi_y^{(0)}$ from its initial value to $\pi/2 \pm 0.156(5)\pi$ and subsequently increasing the short lattice depth to $V_{s,y} = 40(1)E_{r,s}$. In this lattice configuration, ground-state atoms on singly and doubly occupied plaquettes are fully localized on the lower-lying site along y , owing to the large double-well tilt Δ_y and the suppression of tunnelling as $J_y \delta J_y \rightarrow 0$. On the other hand, atoms in the excited band along y localize on the higher-lying site and can be detected directly by measuring the resulting double-well imbalance.

Detecting doubly occupied plaquettes. The doublon fraction can be determined by taking advantage of the fact that two atoms in the same double well localize on the lower-lying site only at much larger double-well tilts than for a single atom, owing to the repulsive on-site interaction. For this, the double wells along y are first merged into a single site by removing the short lattice and increasing the long lattice to $V_{l,y} = 30(1)E_{r,l}$ within 5 ms. At the same time, the orthogonal lattice depths are ramped up to $V_{s,x} = 70(2)E_{r,s}$ and $V_z = 100(3)E_{r,z}$ to increase the interaction energy. After that, $\varphi_y^{(0)}$ is shifted adiabatically to either $0.474(5)\pi$ or $0.431(5)\pi$ and the sites are again split into double wells by ramping up the short lattice to $V_{s,y} = 40(1)E_{r,s}$. At $\varphi_y^{(0)} = 0.431\pi$, single atoms and doublons are both fully localized on the lower-lying site. On the other hand, at $\varphi_y^{(0)} = 0.474\pi$, single atoms are still very well localized on the lower site, but two atoms in the same double well localize on different sites owing to the large interaction energy $U > \Delta_y$. By determining the site occupations for both phases, we can therefore infer the doublon fraction from the difference in the even-odd imbalance between the two measurements.

Calculating the double-well imbalance along y . The measurement of the population imbalance in the y direction as a function of φ_x for Figs 3 and 4 is performed after an integer or half-integer number of pump cycles ($\varphi_x = l\pi$, $l \in \mathbb{Z}$). At these points, the superlattice along x is in the staggered configuration, with the maximum energy offset $|\Delta_x| \gg J_x$ and $\delta J_x = 0$. The atoms are thus fully localized on either even

or odd sites along x for $\varphi_x = 2l\pi$ or $\varphi_x = (2l+1)\pi$, respectively. The four-site unit cell of the 2D superlattice therefore effectively reduces to a double well along y .

For singly occupied double wells, the expected imbalance in the y direction for atoms in the ground ($\mathcal{I}_y^{\text{gs}}$) and first excited state ($\mathcal{I}_y^{\text{exc}}$) can then be calculated from the single-particle double-well Hamiltonian

$$\hat{H}_{\text{DW}}^{(1)}(\varphi_y) = \begin{pmatrix} \Delta_y(\varphi_y)/2 & -J_y^0(\varphi_y) \\ -J_y^0(\varphi_y) & -\Delta_y(\varphi_y)/2 \end{pmatrix} \quad (5)$$

with $J_y^0(\varphi_y) = J_y(\varphi_y) + \delta J_y(\varphi_y)/2$ and using the Fock basis for the atoms on even and odd sites, $|1, 0\rangle$ and $|0, 1\rangle$, respectively.

Correspondingly, the imbalance for the ground state of a doubly occupied double well ($\mathcal{I}_y^{2\text{-gs}}$) can be determined using the two-particle double-well Hamiltonian

$$\hat{H}_{\text{DW}}^{(2)}(\varphi_y) = \begin{pmatrix} U + \Delta_y & -\sqrt{2}J_y^0 & 0 \\ -\sqrt{2}J_y^0 & 0 & -\sqrt{2}J_y^0 \\ 0 & -\sqrt{2}J_y^0 & U - \Delta_y \end{pmatrix} \quad (6)$$

in the Fock basis $\{|2, 0\rangle, |1, 1\rangle, |0, 2\rangle\}$. Here, U denotes the on-site interaction energy for two atoms localized on the same lattice site.

Fit function for nonlinear response. On the basis of the above model, the experimental data are fitted with the function $\mathcal{I}_y(\varphi_x) + \mathcal{I}_0$ with $\varphi_y \rightarrow \varphi_y^{\text{exp}} = \varphi_y^{(0)} + \alpha(\varphi_y - \varphi_y^{(0)})$. The two fit parameters are the pre-factor α , which describes the change in the superlattice phase along y with φ_x , compared to the ideal case $\varphi_y^{\text{exp}} = \varphi_y$, and an overall offset \mathcal{I}_0 . The transport properties of the lowest band are encoded in the slope of the ground-state imbalance at $\varphi_x = 0$. Knowing α , it can be related to the ideal slope via

$$\frac{\partial \mathcal{I}_y^{\text{gs}}(\varphi_y^{\text{exp}})}{\partial \varphi_x} = \frac{\partial \mathcal{I}_y^{\text{gs}}(\varphi_y^{\text{exp}})}{\partial \varphi_y^{\text{exp}}} \frac{\partial \varphi_y^{\text{exp}}}{\partial \varphi_x} = \alpha \frac{\partial \mathcal{I}_y^{\text{gs}}(\varphi_y)}{\partial \varphi_x}$$

Per cycle, this gives a change in the population imbalance for ground-state atoms of

$$\delta \mathcal{I}_y^{\text{gs}} = \alpha \left[\mathcal{I}_y^{\text{gs}}(\varphi_y) \Big|_{\varphi_x=2\pi} - \mathcal{I}_y^{\text{gs}}(\varphi_y) \Big|_{\varphi_x=0} \right]$$

Determining the second Chern number from the scaling of the nonlinear response with θ .

The COM displacement per cycle along y for an infinite system, $\delta y_{\text{COM}} = \nu_2 \theta a_x a_y / d_{1y}$, scales linearly with the perturbing angle θ . The second Chern number can thus be extracted from the slope of $\delta y_{\text{COM}}(\theta)$. Having confirmed that the measured shape of $\delta \mathcal{I}_y^{\text{gs}}(\varphi_y^{(0)})$ is the same as expected theoretically, the response of an infinite system at a given angle θ can be inferred from a single measurement of $\delta \mathcal{I}_y^{\text{gs}}$ at a fixed $\varphi_y^{(0)}$. This holds for all angles because the shape of $\overline{\mathcal{I}}(\varphi_y^{(0)})$ is independent of θ . To obtain ν_2 , it is therefore sufficient to determine the slope of $\delta \mathcal{I}_y^{\text{gs}}(\theta)$ at a constant $\varphi_y^{(0)}$.

Nonlinear response versus lattice depth. The technique for detecting the nonlinear response with site-resolved band mapping, introduced in the main text, allows us to determine the slope over a wide range of lattice parameters accurately. To demonstrate this, we measure the slope of the nonlinear response at $\varphi_y^{(0)} = 0.500(5)\pi$ and $\theta = 0.54(3)$ mrad for various values of the transverse short-lattice depth $V_{s,y}$ (Extended Data Fig. 1). As expected, the slope increases with larger depths as the band gap decreases and the Berry curvature Ω^y becomes more and more localized around $\varphi_y^{(0)} = (l + 1/2)\pi$ with $l \in \mathbb{Z}$.

At $V_{s,y} = 6.25E_{\text{rs}}$, the first and second excited subbands along y touch for $\varphi_y^{(0)} = l\pi$, leading to a topological transition where the signs of the first and second Chern number of the first excited subband change from $+1$ for $V_{s,y} < 6.25E_{\text{rs}}$ to -1 for $V_{s,y} > 6.25E_{\text{rs}}$. This corresponds to a transition between the Landau and Hofstadter regimes²⁵. For the lowest band, the two regimes are topologically equivalent and the atoms therefore move in the same direction. In both limits, the

experimentally determined slope matches very well with the one expected in an ideal system. This nicely illustrates that the transport properties of the lowest band can be extracted correctly in both regimes, even in the presence of atoms in the first excited band.

Alignment of the tilted superlattice. Each optical lattice is created by retroreflecting a laser beam, which is focused onto the atoms by a lens on either side of the cloud. For the superlattices, the incoming beams of the short and long lattices are overlapped using a dichroic mirror in front of the first lens. To control the tilt angle θ of the long lattice along y , a glass block is placed in the beam path before the overlapping. By rotating this glass block, a parallel displacement of the incoming beam can be induced, which is then converted into an angle θ relative to the short lattice beam at the first lens. The two beams intersect at the focus point of the lens, which corresponds to the position of the cloud of atoms. After passing through the second lens behind the cloud, both beams are retroreflected by the same mirror. The counter-propagating beams travel along the paths of the incoming beams, thereby creating the lattice potentials with the same relative angle θ .

Determining the angle θ . When the long lattice in the y direction is tilted by an angle θ with respect to the short lattice, the phase of the superlattice along y depends on the position along x . This leads to a modification of the on-site potential, which for small angles can be approximated as a linear gradient along the x axis, pointing in opposite directions on even and odd sites in y

$$\Delta_y^{m,y}(\varphi_y) \approx \Delta_y^{m,y}(\varphi_y^{(0)}) + (-1)^m y \delta m_x$$

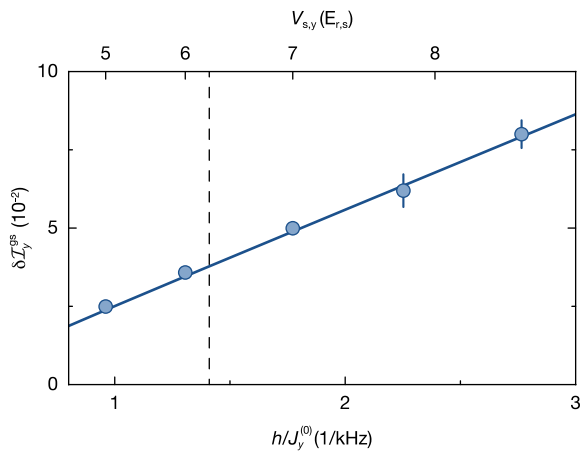
The strength of the gradient is

$$\delta = \left. \frac{\pi d_s}{d_1} \frac{\partial \Delta_y}{\partial \varphi_y} \right|_{x=0} \theta$$

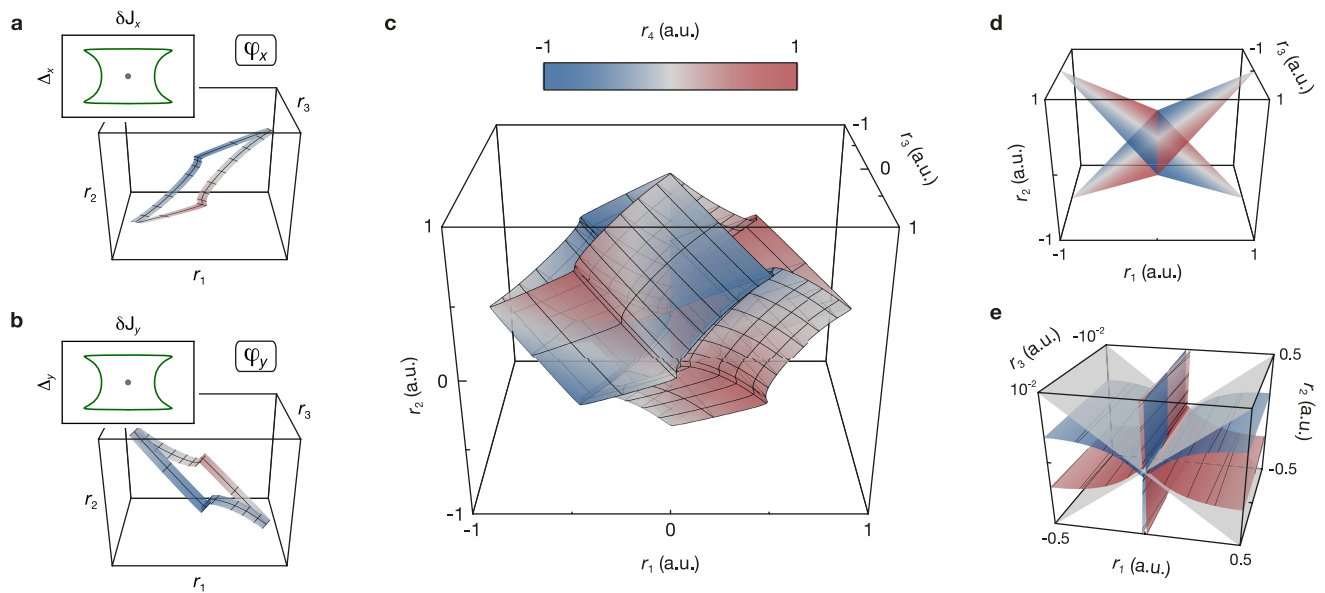
for a given superlattice phase $\varphi_y^{(0)}$ and can therefore be used to determine θ . To do this in the experiment, a superfluid is prepared at $\mathbf{k} = \mathbf{0}$ in a 2D lattice with $V_{s,x} = 13.0(4)E_{\text{rs}}$ and $V_{1,y} = 10.0(3)E_{\text{r1}}$. After increasing $V_{1,y}$ to $70(2)E_{\text{r1}}$ within 0.2 ms, the lattice sites are split along y by ramping up the short lattice in the y direction to $V_{s,y} = 20.0(6)E_{\text{rs}}$ in 0.4 ms. The superlattice phase $\varphi_y^{(0)}$ is set to either $0.344(5)\pi$ or $0.656(5)\pi$ such that the atoms fully localize on even or odd sites along y , respectively. The resulting Bloch oscillations that are induced by the gradient are probed by measuring the momentum distribution of the atoms after a variable hold time. The angle θ is then calculated from the average Bloch oscillation period of both phases to minimize the influence of additional residual gradients.

Data availability. The data that support the findings of this study are available from the corresponding author on reasonable request.

- Xiao, D., Chang, M.-C. & Niu, Q. Berry phase effects on electronic properties. *Rev. Mod. Phys.* **82**, 1959–2007 (2010).
- Harper, P. G. The general motion of conduction electrons in a uniform magnetic field, with application to the diamagnetism of metals. *Proc. Phys. Soc. A* **68**, 879–892 (1955).
- Azbel, M. Ya. Energy spectrum of a conduction electron in a magnetic field. *Zh. Eksp. Teor. Fiz.* **46**, 929–946 (1964); *Sov. Phys. JETP* **19**, 634–645 (1964) [transl.].
- Hofstadter, D. R. Energy levels and wave functions of Bloch electrons in rational and irrational magnetic fields. *Phys. Rev. B* **14**, 2239–2249 (1976).
- Hatsugai, Y. & Kohmoto, M. Energy spectrum and the quantum Hall effect on the square lattice with next-nearest-neighbor hopping. *Phys. Rev. B* **42**, 8282–8294 (1990).
- Roux, G. *et al.* Quasiperiodic Bose–Hubbard model and localization in one-dimensional cold atomic gases. *Phys. Rev. A* **78**, 023628 (2008).
- Marra, P., Citro, R. & Ortix, C. Fractional quantization of the topological charge pumping in a one-dimensional superlattice. *Phys. Rev. B* **91**, 125411 (2015).
- Widera, A. *et al.* Coherent collisional spin dynamics in optical lattices. *Phys. Rev. Lett.* **95**, 190405 (2005).
- Gerber, F., Widera, A., Fölling, S., Mandel, O. & Bloch, I. Resonant control of spin dynamics in ultracold quantum gases by microwave dressing. *Phys. Rev. A* **73**, 041602 (2006).



Extended Data Figure 1 | Nonlinear response versus depth of the short lattice along y . Slope of the nonlinear response at $\varphi_y^{(0)} = 0.500(5)\pi$ and $\theta = 0.54(3)$ mrad as a function of $V_{s,y}$, with all other lattice parameters as in Figs 3 and 4. $J_y^{(0)} = J_y(\varphi_y^{(0)}) + \delta J_y(\varphi_y^{(0)})/2$ with $\varphi_y^{(0)} = \pi/2$ is the maximum intra-double-well tunnelling rate along y , which is calculated from the corresponding lattice depth. The solid line indicates the theoretically expected slope and the error bars show the fit error for the slope. The dashed line at $V_{s,y} = 6.25E_{r,s}$ marks the point at which a topological transition occurs in the first excited subband along y , indicating the transition between the Landau regime for $V_{s,y} < 6.25E_{r,s}$ and the Hofstadter regime for $V_{s,y} > 6.25E_{r,s}$.



Extended Data Figure 2 | Pump cycle of the 2D topological charge pump. The 4D tight-binding parameter space $(\delta J_x, \Delta_x, \delta J_y, \Delta_y)$ is visualized using the transformation in equation (4). **a**, Changing the pump parameter φ_x leads to a periodic modulation of δJ_x and Δ_x along a closed trajectory, as shown in the inset for a full pump cycle $\varphi_x = 0 \rightarrow 2\pi$. This pump path (green) encircles the degeneracy point at the origin (grey), at which the gap between the two lowest subbands of the Rice–Mele model closes. The surface in the main plot shows the same trace transformed according to equation (4) and with $\varphi_y \in [0.46\pi, 0.54\pi]$. The spacing of the mesh grid illustrating φ_x is $\pi/10$. **b**, For a given φ_x , a large system simultaneously samples all values of φ_y . This corresponds to a closed path

in δJ_y – Δ_y parameter space, in which a singularity also occurs at the origin (inset). The main plot shows the transformed path for $\varphi_x \in [0.46\pi, 0.54\pi]$. **c**, In a full pump cycle, such a system therefore covers a closed surface in the 4D parameter space by translating the path shown in **b** along the trajectory from **a**. **d**, In the transformed parameter space, the singularities at $(\delta J_x = 0, \Delta_x = 0)$ and $(\delta J_y = 0, \Delta_y = 0)$ correspond to two planes that touch at the origin. **e**, Cut around $r_3 = 0$ showing both the pump path from **c** (red/blue) and the singularities from **d** (grey). Whereas they intersect in the 3D space (r_1, r_2, r_3) , the value of r_4 is different on both surfaces and the 4D pump path thus fully encloses the degeneracy planes.